Journal of Applied Fluid Mechanics, Vol. 17, No. 1, pp. 159-175, 2024.
Available online at www.jafmonline.net, ISSN 1735-3572, EISSN 1735-3645.
https://doi.org/10.47176/jafm.17.1.2010

A Numerical Study on the Energy Dissipation Mechanisms of a Two-Stage Vertical Pump as Turbine Using Entropy Generation Theory

T. P. Chen[1,2†], X. Z. Wei[1], R. S. Bie[2], Y. Li[1], T. Zhang[1,2] and Y. X. Liu[1,3]

[1] *State Key Laboratory of Hydro-Power Equipment, Harbin Institute of Large Electric Machinery, Harbin 150040, China*
[2] *School of Energy Science and Engineering, Harbin Institute of Technology, Harbin 150001, China*
[3] *College of Power and Energy Engineering, Harbin, Harbin Engineering University, Harbin 150000, China*

†*Corresponding Author Email: chentp@hec-china.com*

ABSTRACT

Utilizing a two-stage vertical pump as turbine (TVPAT) is an economically method for constructing small-scale pumping and storage hydropower stations at high head-low discharge sites, such as underground coal mines. The energy dissipation mechanisms in flow passages are theoretically important for performance prediction and geometric parameter optimization. In this paper, the energy dissipation within the TVPAT has been studied using entropy generation theory, which can be applied to visual, locate and quantify energy dissipation. The numerical solution of entropy dissipation components was extracted on turbine modes in different flow rates using the steady-state single-phase SST *k*-*ω* turbulence model. The numerical results show that the energy dissipation in TVPAT mainly comes from turbulent fluctuation (43.6%-72.1%) and blade surface friction (27.8%-58.2%). The runners are the main source of turbulent entropy ($S_{D'}$) generation (47.2%-83.3%). The contribution of the return channel and spiral case to the $S_{D'}$ generation under overload conditions is significant, accounting for 33.6% and 14.3 at 1.3$Q_{BEP,}$ respectively. Flow field analysis reveals that high $S_{D'}$ generation within a runner are located in the striking flow region of the leading edge, the flow squeezing region in the blade channel, and the wake region of tailing edge. The mismatch between the placement angle of the blades or guide vanes and the liquid flow angle is an important incentive for $S_{D'}$ generation. Moreover, hydraulic energy is consumed through the interaction between mainstream and local inferior flows such as separation and vortices, as well as the striking and friction between local fluid and wall surfaces.

Article History

Received May 14, 2023
Revised August 16, 2023
Accepted September 12, 2023
Available online November 1, 2023

Keywords:

Pump as turbine
Two-stage
Energy dissipation
Entropy generation theory
Pumping and storage

1. INTRODUCTION

Pumped storage is currently the most mature and economical energy storage method. However, the construction period of large pumping and storage hydropower stations (PSHTs) is long, generally taking 8 to 10 years. Meanwhile, the pump turbine of the energy conversion unit needs to be specially designed. The small-scale PSHT can be quickly built, provide benefits and improve the quality of power supply at the end of the grid, which can promote the consumption of renewable energy nearby. However, low cost hydraulic and electric equipment need to implemented to the small-scale PSHT to make it economically feasible. This will eventually result in the emergence of ideas, such as using reverse-run hydraulic pumps at these sites (Jain & Patel, 2014). The concept of a pump as turbine (PAT) can be traced back to 1930 (Williams 1996; Binama et al. 2017). In theory, the field applications of single-stage centrifugal, multistage centrifugal and axial flow pumps as turbines can be compared with Francis, Pelton and Kaplan turbines respectively (Derakhshan & Nourbakhsh, 2008a).

To date, in many studies on PAT, a single-stage centrifugal pump was selected as the research object (Williams 1994; Fernandez et al. 2004; Derakhshan & Nourbakhsh 2008b; Singh & Nestmann, 2010; Nautiyal et al. 2011; Barbarelli et al. 2017). However, single-stage PAT cannot be applied to sites with high head-low discharge, i.e. a pump specific speed of $n \cdot Q^{0.5}/H^{0.75} < 20$ (rpm, m^3/s, m), such as underground coal mines (Blomquist et al. 1979). Since the hydraulic head is shared by two runners, the two-stage vertical centrifugal pump can solve the above problems. Moreover, this pump has a compact structure and low noise, and operates smoothly. According to the construction and use function,

NOMENCLATURE			
S_W	blade surface friction	Q_t	turbine flow rate
$S_{\bar{D}}$	viscous dissipation	$S_{D'}$	turbulent dissipation
$\dot{S}_D'''$	specific entropy	Q_{BEP}	flow rate at best efficiency operation
μ	dynamic viscosity	ω	turbulent eddy frequency
ε	turbulent energy dissipation rate	ρ	density of the fluid
T	temperature	Abbreviations	
k	turbulent kinetic energy	TVPAT	Two-Stage Vertical Pump As Turbine
n	rotation speed	PSHT	Pumping And Storage Hydropower Stations
H_p	pump head	PAT	Pump As Turbine
Q_p	pump flow rate	Subscripts	
τ	shaft torque	t	turbine model
H_t	turbine head	p	pump model

the two-stage vertical pump as turbine (TVPAT) can be completely regarded as an unregulated pump turbine (Blomquist et al. 1979).

The flow energy dissipation mechanism is theoretically important in energy performance prediction and geometric parameter optimization. The energy performance including the power, head, and efficiency is the data that must be analyzed before applying PAT, however, such date cannot be obtained from the manufacturer. Therefore, in early studies mainly predicting the characteristic curves in the reverse mode based on the best efficiency points (BEPs) of pumps (Barrio et al. 2010; Yang et al. 2012; Huang et al. 2017) or the pump specific speeds (Nautiyal & Kumar, 2010; Wang et al. 2017; Pugliese et al. 2021) is mainly focus on. However, due to the lack of understanding in the energy dissipation mechanism, theoretical prediction methods may only be used to obtain a rough picture of the required PAT characteristics. With the support of CFD technology, the research of predecessors confirmed that the energy dissipation of the flow passage is related to the inferior flow. Based on the characterization of pressure and streamlines, Lee et al. (2016) and Maleki et al. (2020) investigated the flow characteristics of multistage PAT return channels. The authors observed an undesirable vortex structure in the diffuser and the return channel. By eliminating obvious undesirable flow regimes, the efficiency of modern pumps is improved. However, further improving the efficiency is difficult because it is hard to visualize, locate and quantify flow energy dissipation.

The entropy generation theory defined by Kock & Herwig (2004) is used to investigate the energy dissipation mechanism. Compared with pressure drop calculation method, it can be used to determine the amount and location of energy dissipation. The entropy generation theory was first applied to turbomachinery by Gong et al. (2013) to determine the quantity and location of losses within a Francis turbine. Since then, entropy generation theory has been applied for the hydraulic loss analysis of different types of fluid machinery, such as wells turbines (Shehata et al. 2016), cyclone separators (Ghorani et al. 2020), pumps (Zhu et al. 2023, Qian et al. 2019), and pump turbines (Li et al. 2016; Gong et al. 2017). Ghorani et al. (2020) numerically used the entropy generation theory to study the irreversible energy losses within the single stage centrifugal PAT for the first time. Lin et al. (2021) performed a similar study with a single stage centrifugal PAT as the research object. Yang et al. (2021) studied the flow loss mechanism at the pump operation of a three-stage electrical submersible pump using entropy production theory. To the best of our knowledge, the energy dissipation mechanism of a two-stage vertical pump in turbine mode investigated using entropy generation theory has not yet been reported.

In this paper, numerical analysis based on entropy generation theory was performed on the reverse mode of a vertical single suction two-stage centrifugal pump to achieve the following objectives:

(1) The energy dissipation characteristics in the flow passage of the TVPAT are revealed under varied operation conditions.

(2) Some clues for the establishment of a prediction model and the optimization design of the structural parameters of the TVPAT is provided.

The article is divided into the following parts: First, the entropy generation theory is introduced. Subsequently, numerical simulation was performed using ANSYS-CFX 2020R1 software and the results were validated by experimental data. The numerical solution of entropy dissipation components was extracted for turbine modes in different flow rates using the steady-state single-phase SST turbulence model. Finally, some conclusions were obtained.

2. CALCULATION OF THE ENTROPY GENERATION

According to the second law of thermodynamics, entropy generation always occurs in an actual flow system. Ignoring the influence of temperature, entropy generation in the working process of fluid machinery, such as pumps, inevitably comes from viscosity and Reynolds stress (Gong et al. 2013).

Considering the flow incompressibility, the specific entropy for laminar flows is given in Eq. (1):

$$\dot{S}_D''' = 2\frac{\mu}{T}\left[\left(\frac{\partial u_1}{\partial x_1}\right)^2 + \left(\frac{\partial u_2}{\partial x_2}\right)^2 + \left(\frac{\partial u_3}{\partial x_3}\right)^2\right] + \frac{\mu}{T}\left[\left(\frac{\partial u_2}{\partial x_1} + \frac{\partial u_1}{\partial x_2}\right)^2 + \left(\frac{\partial u_3}{\partial x_1} + \frac{\partial u_1}{\partial x_3}\right)^2 + \left(\frac{\partial u_2}{\partial x_3} + \frac{\partial u_3}{\partial x_2}\right)^2\right] \quad (1)$$

where $\dot{S}_D'''$ is the specific entropy; μ is the dynamic viscosity; and T is the temperature. Regarding turbulent flow, the specific entropy can be separated into the following two terms by the Reynolds time averaged method: the averaged term ($\dot{S}_{\bar{D}}'''$), and the is fluctuating term ($\dot{S}_{D'}'''$).

$$\dot{S}_D''' = \dot{S}_{\bar{D}}''' + \dot{S}_{D'}''' \tag{2}$$

$$\dot{S}_{\bar{D}}''' = 2\frac{\mu}{T}\left[(\frac{\partial \bar{u}_1}{\partial x_1})^2 + (\frac{\partial \bar{u}_2}{\partial x_2})^2 + (\frac{\partial \bar{u}_3}{\partial x_3})^2\right] + \frac{\mu}{T}\left[(\frac{\partial \bar{u}_2}{\partial x_1} + \frac{\partial \bar{u}_1}{\partial x_2})^2 + (\frac{\partial \bar{u}_3}{\partial x_1} + \frac{\partial \bar{u}_1}{\partial x_3})^2 + (\frac{\partial \bar{u}_2}{\partial x_3} + \frac{\partial \bar{u}_3}{\partial x_2})^2\right] \tag{3}$$

$$\dot{S}_{D'}''' = \frac{\mu}{T}\left\{2\left[(\frac{\partial u_1'}{\partial x_1})^2 + (\frac{\partial u_2'}{\partial x_2})^2 + (\frac{\partial u_3'}{\partial x_3})^2\right] + (\frac{\partial u_2'}{\partial x_1} + \frac{\partial u_1'}{\partial x_2})^2 + (\frac{\partial u_3'}{\partial x_1} + \frac{\partial u_1'}{\partial x_3})^2 + (\frac{\partial u_2'}{\partial x_3} + \frac{\partial u_3'}{\partial x_2})^2\right\} \tag{4}$$

The averaged term ($\dot{S}_{\bar{D}}'''$) can be calculated by post-processing of the velocity field data. However, the fluctuating term ($\dot{S}_{D'}'''$) cannot be obtained directly. Based on investigations by Kock & Herwig (2004) and Herwig et al. (2007), the fluctuating term is closely related to the turbulent model used in the calculation. Therefore, the ($\dot{S}_{D'}'''$) is defined in Eq. (5), where, ε and ρ are the turbulent energy dissipation rate and the density of the fluid, respectively. For the SST k-ω turbulent model, the turbulent entropy generation rate can be achieved by Eq. (6).

$$\dot{S}_{D'}''' = \frac{\rho\varepsilon}{T} \tag{5}$$

$$\dot{S}_{D'}''' = \beta \cdot \frac{\rho\omega k}{T} \tag{6}$$

Where β is an empirical constant, and is equal to 0.09 in the SST k-ω model (Menter, 1994); ω is the turbulent eddy frequency, k is the turbulent kinetic energy.

In addition, the high velocity gradient and pressure gradient existing on the blade surface of rotating fluid machinery triggers a strong wall effect, resulting in non-negligible irreversible energy dissipation (Pei et al. 2016). Hence, the wall entropy generation rate ($\dot{S}_W$) is calculated by Eq. (7) proposed by Hou (Hou et al. 2016).

$$\dot{s}_w = \frac{\vec{\tau}\cdot\vec{v}}{T} \tag{7}$$

Where, $\vec{\tau}$ and $\vec{v}$ is the shear stress in the blade surface, and the velocity of the first grid near the blade surface, respectively.

Hence, the total entropy generation can be achieved by the volume integral of the local entropy generation rate, and the surface integral of the wall entropy generation rate (Eqs. (8~11)).

$$S_{\bar{D}} = \int_V \dot{S}_{\bar{D}}''' dV \tag{8}$$

$$S_{D'} = \int_V \dot{S}_{D'}''' dV \tag{9}$$

$$S_W = \int_A \frac{\vec{\tau}\cdot\vec{v}}{T} dA \tag{10}$$

$$S_{total} = S_{\bar{D}} + S_{D'} + S_W \tag{11}$$

3. NUMERICAL SIMULATION

3.1 Physical Model

In this study, a vertical single-suction two-stage centrifugal pump model with a specific speed of $n \cdot Q^{0.5}/H^{0.75} = 17.12$ (rpm, m^3/s, m) is taken as the research object. The flow and rotation speed at the design point are 137.8 L/s and 850 rpm, respectively. The selection of rotation speed in the study of the energy characteristics of the PAT is consistent with that of pump operation. The two-stage pump is composed of spiral case, first-stage runner, return passage (including forward vanes, and backward vanes), second-stage runner, and draft tube. The geometric model is shown in Fig. 1. The geometric design parameters of the first and second-stage runners are the same, and the spiral case is equipped with fixed guide vanes. The main geometric parameters of the whole passage are shown in Table. 1.

3.2 Governing Equations, Numerical Settings and Boundary Conditions

In this study, the commercial software ANSYS-CFX 2020R1 is used for the numerical calculation of the reverse operation of the pump. The steady Navier-Stokes equation is Reynolds time-averaged by using the finite volume method. The incompressible average motion mass equation and momentum equation are shown in Equations (12) and (13).

$$\frac{\partial u_i}{\partial x_i} = 0 \tag{12}$$

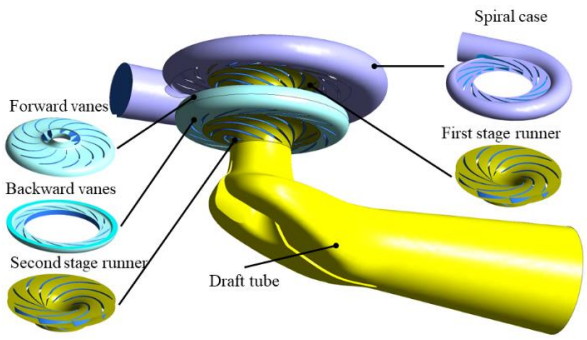

Fig. 1 Schematic map of the flow domain model of the simulated TVPAT

Table 1 Basic parameters

Parameter	Value	Unit
Runner diameter (high-pressure side), D_1	270	[mm]
Runner diameter (low-pressure side), D_2	480	[mm]
Runner blade number, Z	9	[-]
Blade inlet angle, β_1	17.5	[degree]
Blade outlet angle, β_2	13.5	[degree]
Runner blade wrap angle, α	137	[degree]
Spiral case discharge diameter, D_3	230	[mm]
Forward vane number, Z_s	13	[-]
Backward vane number, Z_s	13	[-]
Draft tube discharge diameter, D_4	500	[mm]

$$\frac{\partial U_i}{\partial t} + U_j \frac{\partial U_i}{\partial x_j} = f_i - \frac{1}{\rho}\frac{\partial P}{\partial x_i} + \nu \frac{\partial^2 U_i}{\partial x_j^2} + \frac{1}{\rho}\frac{\partial(-\rho \overline{u_i' u_j'})}{\partial x_j} \tag{13}$$

where u is the velocity, x is the coordinate component, and $-\rho\overline{u_i'u_j'}$ is the is Reynolds stress. It can be seen from the above equation that after the control equation is time-averaged, the pulsating velocity term is added to the control equation to reflect the effect of pulsating velocity on the average motion (Reynolds stress). However, due to the increase in the Reynolds stress, the governing equation is no longer closed. To solve the governing equation, it is necessary to establish the relationship between the Reynolds stress and average motion, namely, the so-called turbulence model. In this paper, the two-equation SST turbulence model is adopted, and its mathematical expressions are Eq. (14) and (15). The SST model integrates *k-ω* and *k-ε*. The two models are solved numerically in different regions through mixed functions. In the boundary layer region, the low Reynolds number model *k-ω* is used for calculation; while in the free shear layer, the high Reynolds number model *k-ε* with good adaptability is used for calculation. The SST model combines the advantages of the two models, making it able to accurately simulate the flow separation of the reverse pressure gradient, and has a good performance for the complex flow field prediction.

$$\frac{\partial(\rho k u_i)}{\partial x_i} = \frac{\partial}{\partial x_i}\left(\Gamma_k \frac{\partial k}{\partial x_j}\right) + \overline{G_k} - Y_k + S_k \tag{14}$$

$$\frac{\partial(\rho \omega u_i)}{\partial x_i} = \frac{\partial}{\partial x_i}\left(\Gamma_\omega \frac{\partial \omega}{\partial x_j}\right) + \overline{G_\omega} - Y_\omega + S_\omega + D_\omega \tag{15}$$

In the CFD simulation process, the spiral case inlet is set as the inlet boundary, and the flow direction is vertical to the surface. The outlet of the draft tube is set as the outlet boundary. The mass flow rate is selected for the inlet boundary, the static pressure is set for the outlet boundary, and the reference pressure is atmospheric pressure. The nonslip boundary condition is adopted for the wall surface. The rotational speed of the runner is set to 850 rpm. A frozen rotor is used to connect the dynamic and static interfaces between the spiral case and runner, between the runner and the return channel and between the runner and draft tube. In the model, the relative position of watersheds is considered on both sides of the interface, and is suitable for flows with relatively large changes in the flow field parameters in the circumferential direction. The runner adopts the full-channel calculation method. The fluid is selected as water at 25 °C, the density is 1000 kg/m^3, and the dynamic viscosity is 0.001 Pa·s.

3.3 Domain Discretization and Accuracy Check

In this paper, the runner passages and the return channel were discretized by structured hexahedron elements. The spiral case and draft tube were discretized by unstructured tetrahedron elements. To verify that the adopted grid density can reasonably predict the internal and external characteristics of the simulated PAT within a certain error range, six sets of grids were selected for verification. The number of grid nodes ranges from 14.5 million to 26.5 million. To evaluate the independence of the numerical solution from the generated grid, the pump hydraulic efficiency (88.95%) at the rated pump discharge was selected as the target parameter.

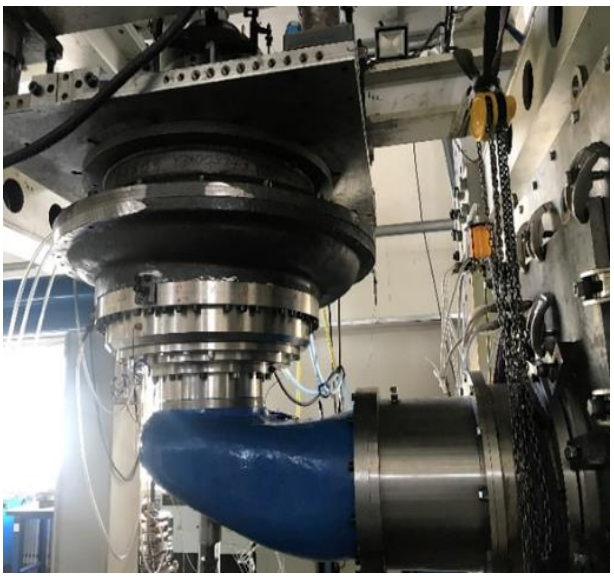

Fig. 2 Test rig on-site

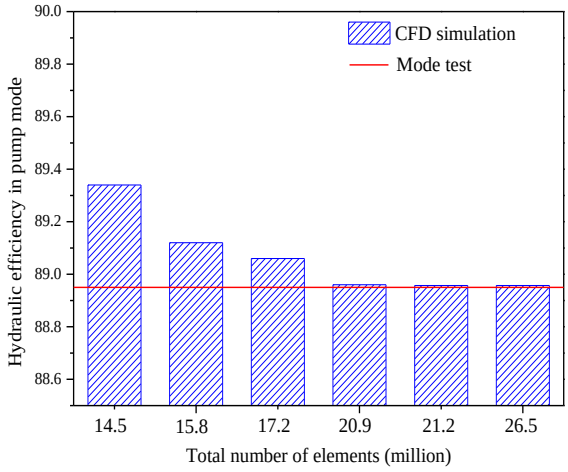

Fig. 3 Pump hydraulic efficiency for different number of mesh elements

Figure 2 shows the model test rig on-site. Model tests were performed on a stand hydraulic machinery test rig at the Harbin Institute of Large Electric Machinery in China. The comprehensive test error for efficiency is less than ±0.2%, and the repeated test error is less than ±0.1%. All measurements were conducted in accordance with the International Electrotechnical Commission (IEC) standard 60193 (International Electrotechnical Commission, 1999). The efficiency η in pump mode can be calculated by Eq. (16)

$$\eta = \frac{\rho g H_p Q_p}{\tau \omega} \times 100 \tag{16}$$

In the above equation, H_p denotes the pump head, Q_p is pump flow rate, τ is shaft torque provided by runners, and ω is rotation angular speed. The results presented in Fig. 3 show that increasing the number of grid cells more than 20.9 million has no remarkable effect on efficiency; The difference between the experimental results and the simulation results is less than 0.01%. Therefore, 21.2 million nodes were finally selected for numerical simulation calculation. The grid details are shown in Table 2 and Fig. 4.

Table 2 Grid Details

Component	Grid node number	Grid element number
Spiral case	2079499	5700338
First-stage runner	4691016	4426506
Forward vane	5803278	5505786
Backward vane	4705974	4462302
Second stage runner	4713390	4456215
Draft tube	1743816	4523386

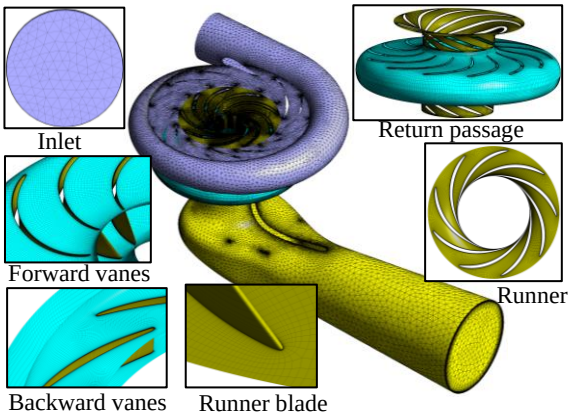

Fig. 4 Schematic map of grid using in CFD simulation

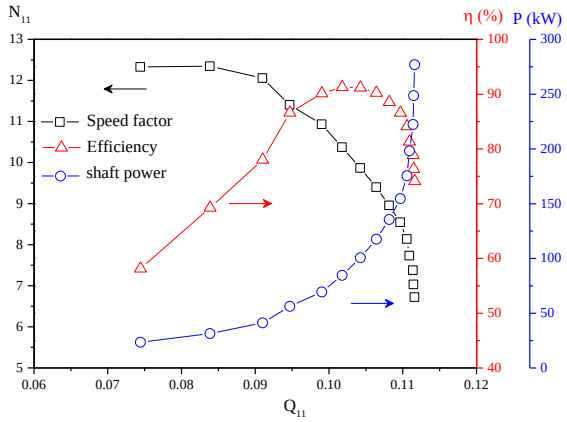

Fig. 5 Energy characteristic curves of the simulated TVPAT

4. RESULTS AND DISCUSSION

4.1 Energy Characteristic Curves in Turbine Mode

Figure 5. shows the energy characteristic curves of the simulated TVPAT, including Planes N_{11}-Q_{11}, P-Q_{11}, and η-Q_{11}, where, N_{11}, Q_{11}, P, and η are the speed factor, discharge factor, shaft power and efficiency, respectively, given by Eqs. (17) ~ (20). In the above equations, H_t denotes the turbine head, and Q_t is the turbine flow rate. When Q_{11} increases from 0.075 to 0.083, N_{11} maintains a constant value of 12.3. Subsequently, N_{11} decreases exponentially to 6.7. The efficiency gradually increases from 25.0% to the maximum of 91.3% as Q_{11} increases from 0.075 to 0.1; however, when the flow continues to increase, the efficiency declines sharply. The shaft power curve rises slowly from 23.5 kW to 41.2 kW in the range of 0.075 ~ 0.091. Then, it rises in an almost vertical straight line. According to the calculation results, the flow

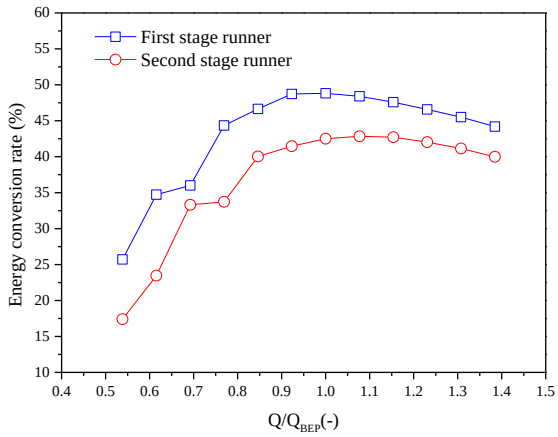

Fig. 6 Energy conversion rates of the first and second-stage runners

and shaft power parameters at the best efficiency point of the simulated TVPAT are 178.6 L/s, and 84 kW, respectively. The flow ratio at the best efficiency operating as a turbine and pump is 178.6/137.8 = 1.29, which is very close to the result of 1.28 obtained by Pugliese (Pugliese et al. 2021).

$$n_{11} = \frac{nD_2}{\sqrt{g \cdot H_t}} \tag{17}$$

$$Q_{11} = \frac{Q_t}{D_2^2\sqrt{g*H_t}} \tag{18}$$

$$P_{shaft} = \tau\omega \tag{19}$$

$$\eta = \frac{\tau\omega}{\rho g H_t Q_t} \times 100 \tag{20}$$

Figure 6 shows the energy conversion rates of the first and second-stage runners. The abscissa is the ratio of mass flow at each operating point to that of the best efficiency point. The energy conversion rate represents the ratio of mechanical energy converted from the runner and input total energy, which is calculated by Eq. (21). In this equation, τ_i is the shaft torque provided by the first-stage runner or second-stage runner. As shown in the figure, the energy conversion rate curves of the first and second-stage runners have the same trend, and the curve of the second-stage is located below that of the first-stage in the whole flow range. The difference in the inflow conditions is the main reason for the dissimilarities in the flow pattern of the runners between stages (Li et al. 2023), which further leads to different output powers of the runners. In addition, the specific energy of the inlet fluid of the first-stage runner is greater than that of the second-stage runner. Thus, the energy conversion rate of the first-stage runner is greater than that of the second-stage runner. When the flow rate increases to the optimum operation, the conversion rates of the first and second-stage runners increase to 48.8% and 42.5% respectively; then, they show a downward trend.

$$\gamma = \frac{\tau_i\omega}{\rho g H_t Q_t} \times 100 \tag{21}$$

4.2 Hydraulic Loss of the Total Flow Passage in the Turbine Model

Figure 7 shows the variation trends of the hydraulic loss with the discharge obtained from entropy generation

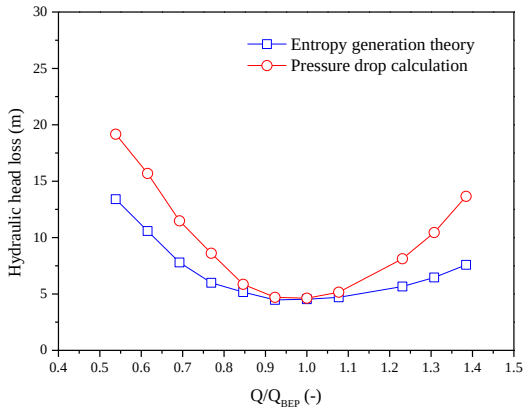

Fig. 7 Variation trends of the hydraulic loss with the discharge obtained from entropy generation theory and pressure drop method respectively

theory (Eq. (22)) and pressure drop method (Eq. (23)). It is found that the calculated results obtained by the two methods have the same trend, that is, the loss under the optimal operation is small. However, under partial loads and overloads, it is large. Meanwhile, the two curves almost coincide near the best efficiency point, but the gap is gradually widened as the flow increases or decreases. The research by Yu et al. (2022) confirmed that the hydraulic loss calculated by entropy theory is lower than the value determined in the experiment, while that calculated by the pressure drop method shows the opposite trend. Based on the above, the calculation results in this paper are considered reasonable and can be used to study the energy dissipation mechanism of the simulated TVPAT.

$$\Delta H = \frac{T \cdot S_{total}}{\rho g} \tag{22}$$

$$\Delta H = \frac{\rho g H_t Q_t - P_{shaft}}{\rho g} \tag{23}$$

The entropy generation theory involves three types of loss mechanisms: viscous dissipation ($S_{\bar{D}}$), turbulent dissipation ($S_{D'}$), and blade surface friction (S_W). The values of all terms are shown in Fig. 8 for different flow rates. Overall, the entropy generation mainly comes from $S_{D'}$ and S_W, and $S_{\bar{D}}$ can be ignored, which is consistent with the literature results (Qian et al. 2019; Yang *et al.* 2021). $S_{D'}$ decreases first and then increases with an increasing flow rate, and the change trend of $S_{D'}$ is relatively gentle near the optimal operation, accounting for 43.6%. At 0.5 Q_{BEP} and 1.4 Q_{BEP}, the $S_{D'}$ term is much larger than the other two terms, accounting for 72.1% and 64.7%, respectively. It should be noted that the proportion of blade surface friction exceeds the turbulent dissipation in the range of 0.8 Q_{BEP} to 1.2 Q_{BEP}, accounting for 58.2% at the best efficiency point. Lin et al. (2021) obtained the result that S_W and $S_{D'}$ account for 35.3% and 64.3%, respectively, at the design flow condition when using entropy generation to analyse a single-stage centrifugal PAT with 6 runner blades. It is speculated that this difference occurred because the simulated TVPAT in this article includes 18 runner blades. In the process of hydraulic optimization, S_W can be reduced by reducing the number of blades or blade wrap angle.

4.3 Entropy Generation of Two-Stage Pump Components in the Turbine Model

The volumetric turbulent entropy generation rates of each component versus the relative flow rate are presented in Fig. 9. The $S_{D'}$ generation rate of the spiral case is positively correlated with the flow. The $S_{D'}$ change trends of runners, forward vanes and draft tube with flow are the same, that is, it decreases first and then increases, but the lowest points are inconsistent. The lowest points of first-stage runner and forward vanes are in the range of 0.8Q_{BEP}~Q_{BEP}, and those of the second-stage runner and draft tube vary gently in the range of Q_{BEP}~1.2Q_{BEP}. The lowest $S_{D'}$ generation condition of the second-stage runner is consistent with the optimal operation of the whole unit. This indicates that to further improve the efficiency, the first- and second-stage runners should be optimized according to their respective inflow conditions. The $S_{D'}$ generation rate of backward vane presents another trend, that is, first increases and then decreases below 0.9Q_{BEP}, and then increases with the flow rate.

Figure 10 shows the proportion of volumetric turbulent entropy generation of each component versus the relative flow rate. Overall, $S_{D'}$ mainly comes from the first and second-stage runners. The proportion sum of

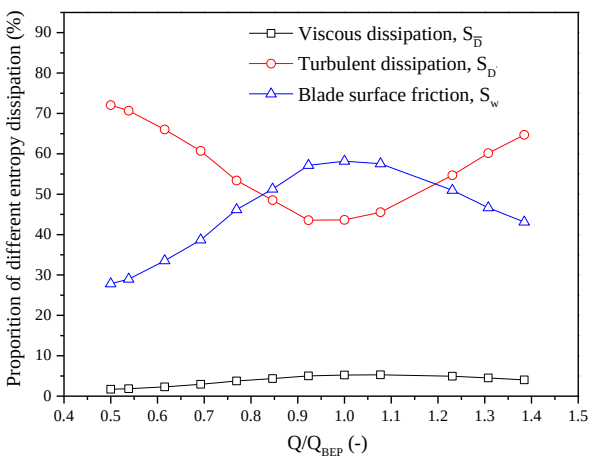

Fig. 8 Changing tendency of three types of entropy yields with relative flow rates

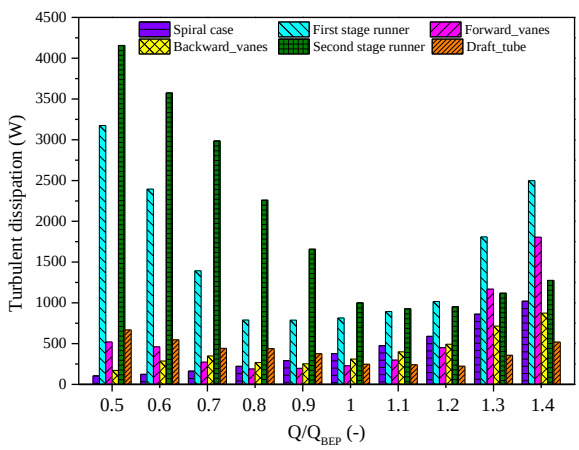

Fig. 9 Volumetric turbulent entropy generation rates of each component versus the relative flow rate

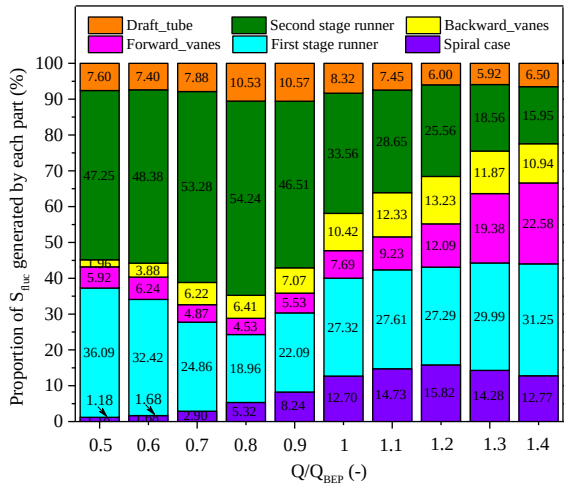

Fig. 10 Proportion of volumetric turbulent entropy generation for each component versus the relative flow rate

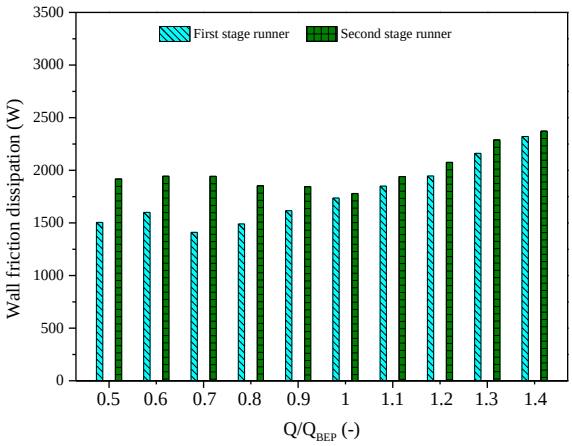

Fig. 11 The S_W generation from the wall effect of runner blade surfaces versus the relative flow rate

both runners decreases from 83.34% to 60.88% by increasing the flow from 0.5Q$_{BEP}$ to Q$_{BEP}$, and decreases to 47.2% as the flow rate further increases to 1.4Q$_{BEP}$. Before 0.8Q$_{BEP}$, the $S_{D'}$ proportion of the first-stage runner decreases first to the minimum value of 18.96 %. Meanwhile, that of second-stage runner increases gradually to the maximum value of 54%. However, after 0.8Q$_{BEP}$, the $S_{D'}$ proportions of the runners exhibit opposite states with changes in the flow rate. Therefore, the energy conversion rate curve of the runner will have a turning point near 0.8, as shown in Fig. 6. In this study, the geometric parameters of the first and second-stage runners are completely consistent. The first-stage runner is located behind the spiral case, and the second-stage runner is located behind the backward vanes. Therefore, the difference in $S_{D'}$ comes from the different inflow conditions at the inlet of the runners. Meanwhile, the two-stage pump used in this study was designed based on the operating requirements of the pump model, without considering the characteristics of reverse operating conditions. Therefore, the minimum value of $S_{D'}$ generation in runner regions does not appear at the best efficiency point. The $S_{D'}$ proportion of the forward vane zone increases rapidly during overload operation, and reachs 22.58% at the 1.3Q$_{BEP}$ condition. This is mainly attributed to the flow pattern at the outlet of the first-stage runner. The trend of the $S_{D'}$ proportion in the backward vane region and the spiral case is the same; that is, $S_{D'}$ proportion increases until the flow reaches 1.3Q$_{BEP}$, and then decreases slightly. The $S_{D'}$ generation from the daft tube has the least variation, ranging from 5.92% to 10.57%. The above details indicate that the focus of geometric parameter optimization during partial load operation should be on the runners, especially the second-stage runner, and during overload operation should be on the return channel and spiral case.

Figure 11 shows the S_W generation of runner blade surfaces versus the relative flow rate. The S_W generation of the first-stage runner maintains a linear increase after the flow rate exceeds 0.7Q$_{BEP}$. The second-stage runner exhibits the same trend when the flow exceeds Q$_{BEP}$. This indicates that the S_W generation is controlled by the flow rate within this range. As described in Eq. (7), S_W is proportional to the velocity gradient. However, it does not follow this pattern before the inflection point (0.7Q$_{BEP}$ or Q$_{BEP}$), and the amplitude of the S_W production change is relatively small. It is speculated that the turbulent structures in the runner passage affect the velocity gradient near the wall surfaces during partial load operations.

4.4 Local Entropy Generation in Two-Stage Pump Components and Flow Field Analysis

The following content will investigate the distribution of $S_{D'}$ generation and flow details of each component, because $S_{D'}$ comes from the inferior flow in the passage, such as flow separation, second flow (Sanghirun & Asvapoositkul, 2023) and cavitation (Li et al. 2018), which can be reduced by local geometric optimization. Meanwhile, the S_W distribution on the runner blade surfaces will also be given. The proportion of $S_{\bar{D}}$ production is very small (<5.3%), so the relevant content will not be provided below.

4.4.1 Spiral Case

Figure 12 shows the $S_{D'}$ and streamline distribution of the spiral case on the horizontal middle section under different flow conditions. As shown in Fig. 12, the $S_{D'}$ of the spiral case mainly comes from the stationary vanes channel and near wall region and gradually increases by increasing the flow. The streamlines in the vane channels are smooth, and there is no obvious inferior flow. Further observation shows that the channel of stationary vanes gradually shrinks in the flow direction, which should be the main reason for $S_{D'}$ generation. The local losses caused by the tapered channel and viscous stress near the wall are proportional to the velocity gradient, so the $S_{D'}$ of the spiral case continues to increase with an increasing flow rate.

4.4.2. First-Stage Runner

The runner is the core component to complete the exchange of hydraulic energy and mechanical energy. To clearly observe the details of energy loss and streamline distribution in the runner, the meridian plane and three

spanwise planes are given as shown in Fig. 13, which are near the runner shroud (Span 0.1), near the hub (Span 0.9), and at the midspan (Span 0.5). Figure 14 shows the contours of the $S_{D'}$ and velocity vector distribution on the meridian plane of the first-stage runner under different flow conditions. As shown in Fig. 14, at a partial load of $0.5Q_{BEP}$, there is a large reflux zone area distributed at the runner inlet, resulting in large energy dissipation. Xia et al. (2017) also found that there was a reflux zone at the runner inlet when studying the flow characteristics of pump-turbine operation in the S zone and interpreted it as flow separation caused by centrifugal force. This should be the inherent characteristic of centrifugal rotating machinery under low flow conditions. At the best efficiency operation, the large $S_{D'}$ region is mainly located near the hub and shroud regions. There is no obvious reflux zone at the inlet, and the streamline isrelatively smooth. At $1.3Q_{BEP}$, energy dissipation near the hub and shroud is significantly higher than that at the best efficiency operation, and the $S_{D'}$ in the channel also increases.

Figure15 demonstrates contours of $S_{D'}$ and streamlines in Span 0.1, 0.5 and 0.9 of the first-stage runner under different flow conditions. overall, the

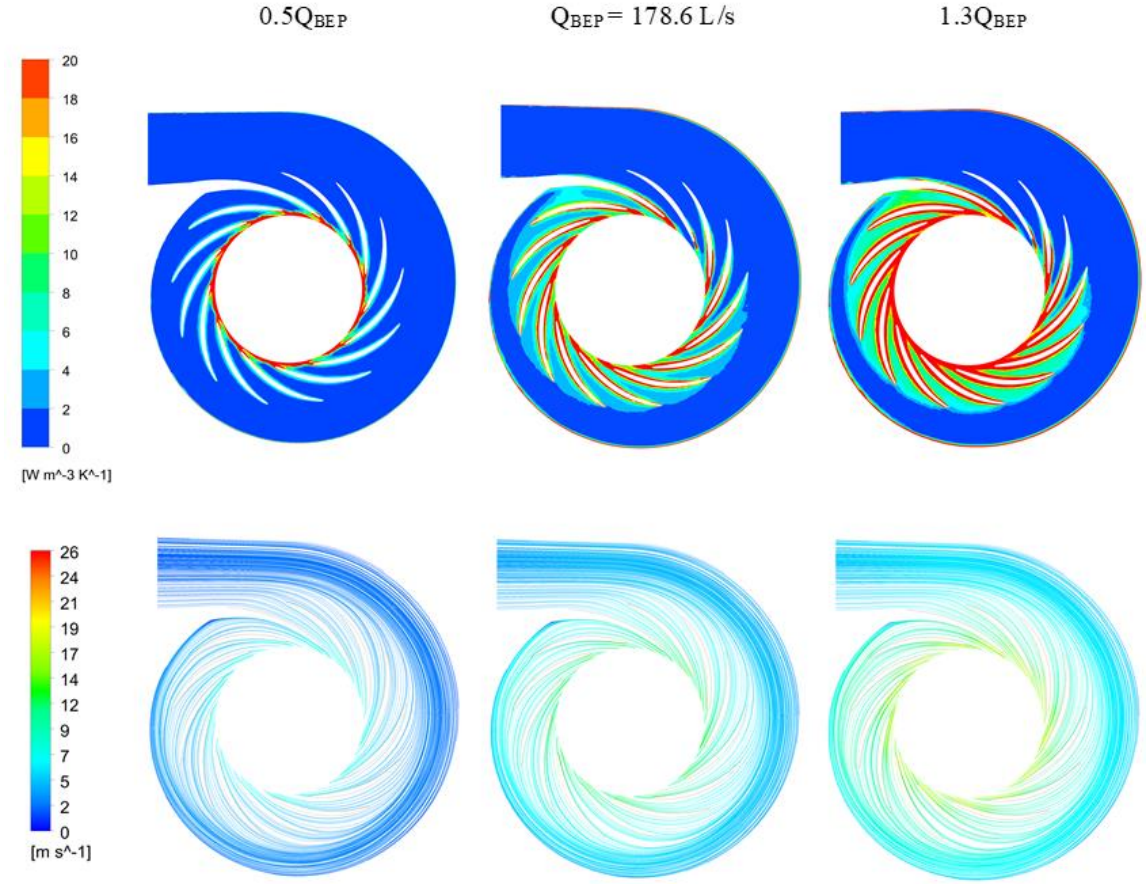

Fig. 12 The $S_{D'}$ and streamline distribution of the spiral case on the horizontal middle section under different flow conditions

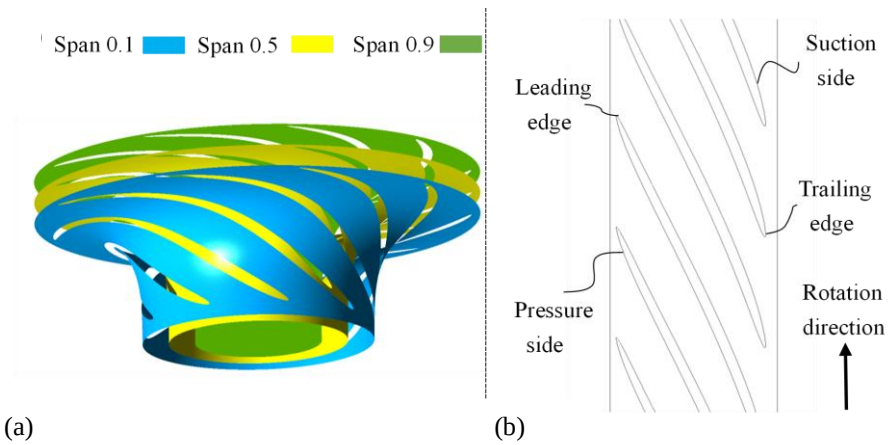

Fig. 13 Location of the leading edge, trailing edge, pressure side and suction side of the runner: (a) spanwise view and (b) cascade view

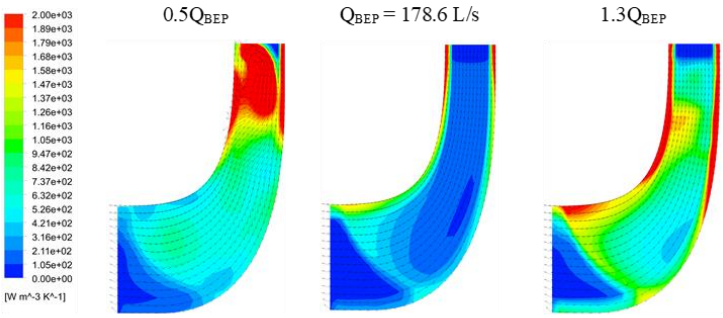

Fig. 14 Contours of the $S_{D'}$ generation and velocity vector distribution on the meridian plane of the first-stage runner under different flow conditions

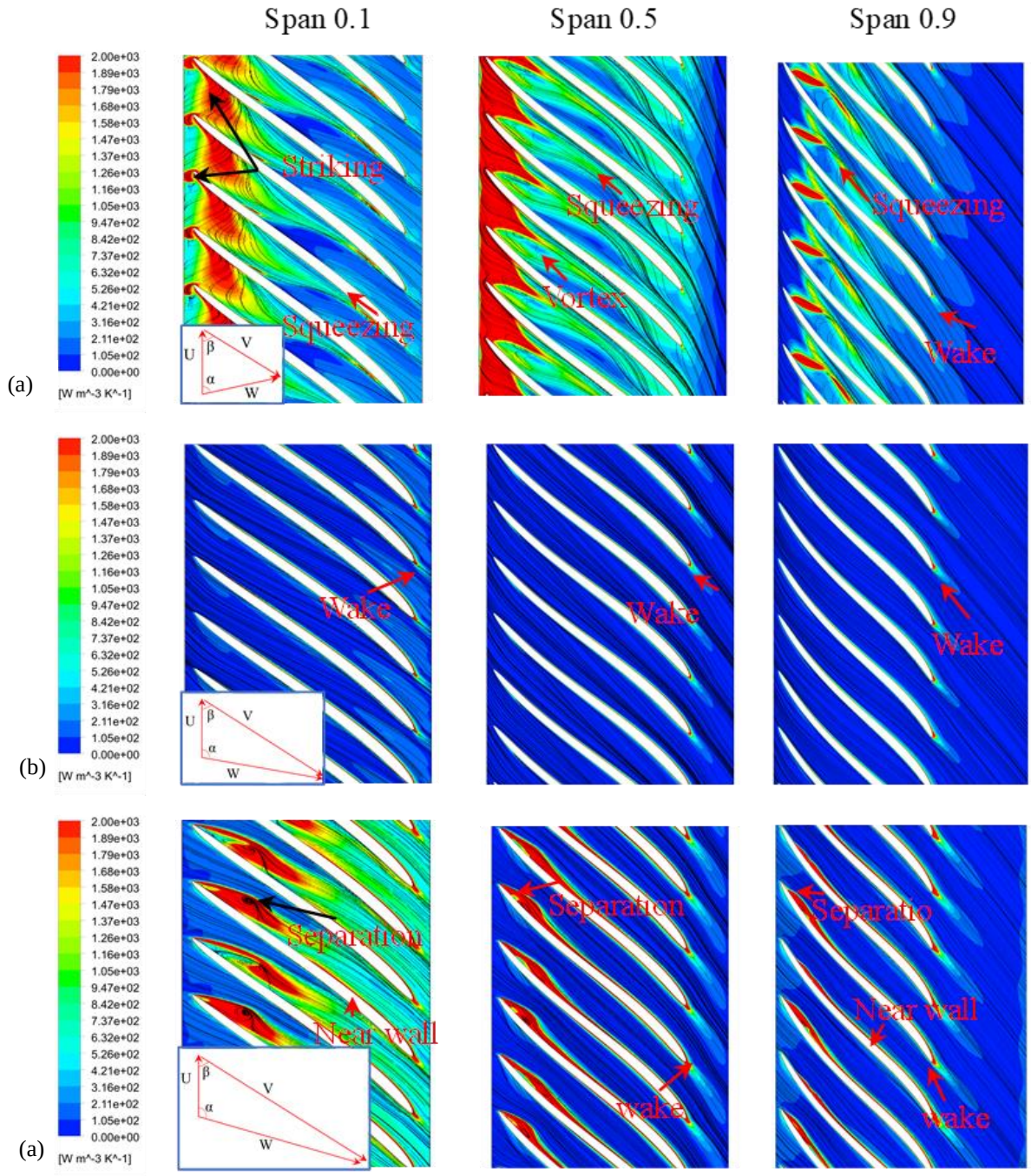

Fig. 15 Contours of the $S_{D'}$ generation and streamlines in span 0.1, 0.5 and 0.9 of the first stage runner at different flow conditions: (a) 0.5Q_{BEP}, (b) Q_{BEP}, and (c) 1.3Q_{BEP}

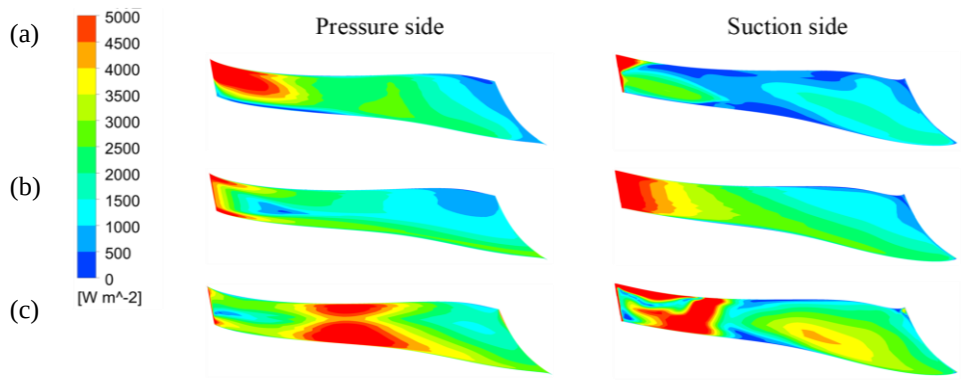

Fig. 16 Entropy production caused by the wall effect on the blade surfaces of the first-stage runner under different flow conditions: (a) 0.5Q_{BEP}, (b) Q_{BEP}, and (c) 1.3Q_{BEP}

turbulence loss in Span 0.9 is smaller than that in the other two spanwise planes under the same operations. Under a partial load of 0.5Q_{BEP}, the $S_{D'}$ generation pattern is complex. High $S_{D'}$ values are mainly located in the striking flow region on the pressure side of the leading edge, the flow squeezing region in the blade channel, and the wake region of the tailing edge of the blades. Meanwhile, the loss at the inlet region in the Span 0.5 surface is greater due to the existence of a reflux zone, as shown in Fig.14. At the best efficiency operation, there is almost no difference in the $S_{D'}$ generation distribution of the three planes. The streamlines flowing through the blade channel are smooth. The $S_{D'}$ is mainly from the wake region. At an overload of 1.3Q_{BEP}, the $S_{D'}$ generation decreases gradually from Span 0.1 to Span 0.9. Large $S_{D'}$ production is mainly in the separation flow region near the suction side and near the wall region of the blades. The energy dissipation mechanism within the runner blade passage can be analysed with the aid of a speed triangle. The speed triangle diagram is given at the lower left corner of Span 0.1 at each flow condition. The direction of the absolute velocity of V at the runner inlet is determined by the outlet placement angle of the stationary vanes in the spiral case, so the included angle of β between the velocities of U and V can be considered to remain unchanged. Under partial load operation, the absolute velocity value is small, so the included angle of α between U and W is small. The fluid impinges on the pressure side of the blade to form striking flow, resulting in a large amount of $S_{D'}$ generation, that causes the streamline to swing towards the suction side of the adjacent blade. At the best efficiency operation, the increase in V is accompanied by an increase in the α angle, and the fluid enters the flow channel almost without collision, Thus, the loss is minimal. Under overload conditions, the α angle further increases, and leads to the formation of flow separation on the suction side of the leading edge, and the wake after flow separation causes large $S_{D'}$ generation. At the same time, due to the increase in the velocity gradient, there is a large $S_{D'}$ generation in the region close to the blade surfaces.

Figure 16 shows the entropy production caused by the wall effect on the blade surfaces of the first-stage runner under different flow conditions. Overall, due to changes in the liquid impact sites, the distribution area of S_W on the pressure side of the blade leading edge decreases with an increasing flow rate, while the opposite pattern is observed on the suction side. The distribution of the S_W production on the middle and rear wall surfaces of the blade is influenced by the local detachment in the channel. As shown in Fig. 15a, under a partial load, detachment occurs near the suction side behind the vortex zone in the runner passage, resulting in minimal S_W generation in the middle section of the blade suction side. Under overload conditions, due to the influences of the wake of the flow separation at the leading edge and the increase in velocity gradient near the wall, there is a significant S_W generation in the middle part of the blade surface.

4.4.3. Return Passage Including Forward Vane and Backward Vane Regions

To explore the return passage turbulent entropy distribution, three spanwise surfaces are defined in the post-processing as shown in Fig. 17, which are near the rotating shaft (Span 0.1), off the rotating shaft (Span 0.9), and at the midspan (Span 0.5). As shown in Fig. 18, overall, the largest $S_{D'}$ generation is at the inlet region of the return passage because the upstream flow direction is forced to change from axial to radial here. The flow quality here is affected by the inlet placement angle of the forward vane and the flow pattern from the outlet of the first-stage runner. At the best efficiency and overload operations, the $S_{D'}$ generation of Span 0.1 at the inlet region is greater than that of Span 0.9, but the opposite is true under partial load conditions. This should be caused by the remarkable effect of centrifugal force at a low flow rate. At the best efficiency operation, the fluid can pass through the forward and backward vane regions relatively smoothly, so the $S_{D'}$ generation in the vanes passage is minimal. Under partial load and overload conditions, due to the mismatch between the inlet placement angle of the forward vane and the liquid flow angle, flow separation occurs in the vane channels, resulting in a large amount of $S_{D'}$ generation in the region near the convex surface of the vanes. Under overload conditions, the streamlines in the inlet region are very disordered, accompanied by a large amount of $S_{D'}$ generation, which indicates that there are complex turbulence structures as shown in Fig. 19c. In the backward vane region, $S_{D'}$ generation mainly occurs in the striking flow region of the leading edge and

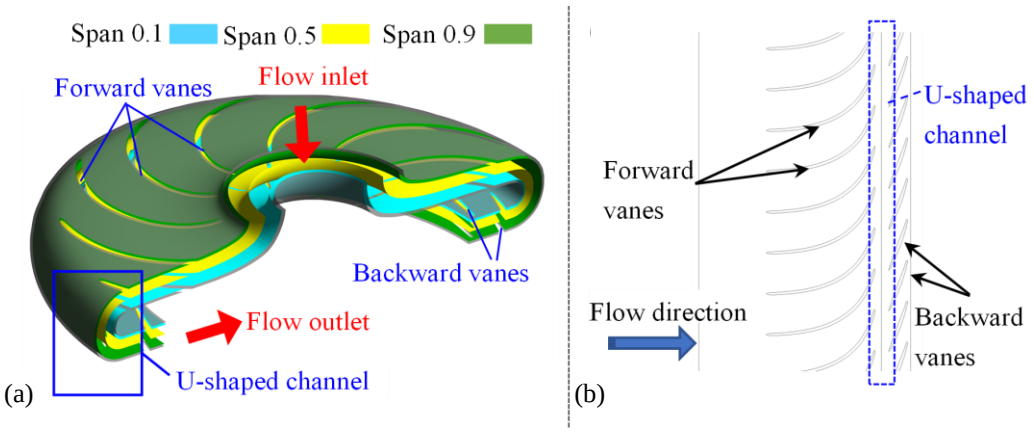

Fig. 17 Position of different span sections of the return passage: (a) spanwise view and (b) cascade view

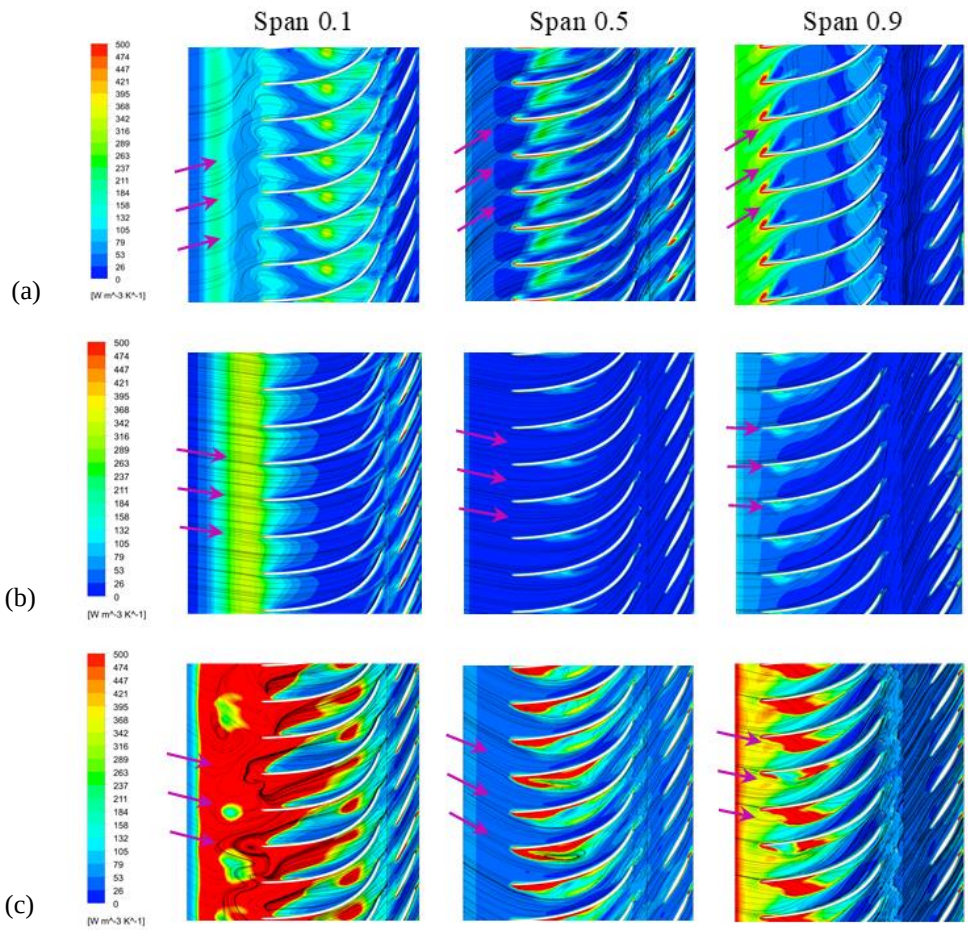

Fig. 18 Contour of the $S_{D'}$ generation and streamlines in Span 0.1, 0.5 and 0.9 of return passage at different flow conditions: (a) 0.5Q$_{BEP}$, (b) Q$_{BEP}$, and (c) 1.3Q$_{BEP}$

the wake region of the tailing edge. The flow from the forward vane outlet is chaotic but becomes relatively stable after flowing through the U-shaped channel. In addition, the length of the backward vanes is relatively short. Therefore, the flow pattern in the backward vane passage is not as complex as that in the forward vane region. Therefore, the contribution of the turbulent structure in the passage between backward vanes to the energy dissipation is smaller than that of the forward vane region. Therefore, the $S_{D'}$ generation in the backward vane zone does not show an increasing trend with a decreasing flow rate under partial load as shown in Fig. 9.

Figure 19 qualitatively shows vortex structures occurring in the forward vane region under different flow condition. Here, the Q-criterion was used to visualize the vortex structures (Günther et al. 2016). The iso-surface of the Q-criterion was set to 500,000 s^{-2}. The tangential velocity of the fluid flowing from of the runner outlet is an important parameter that affects the flow state of the return channel, as shown by the arrow in Fig. 18. As Fig 19. shows, under a partial load of 0.5Q$_{BEP}$, the vortex

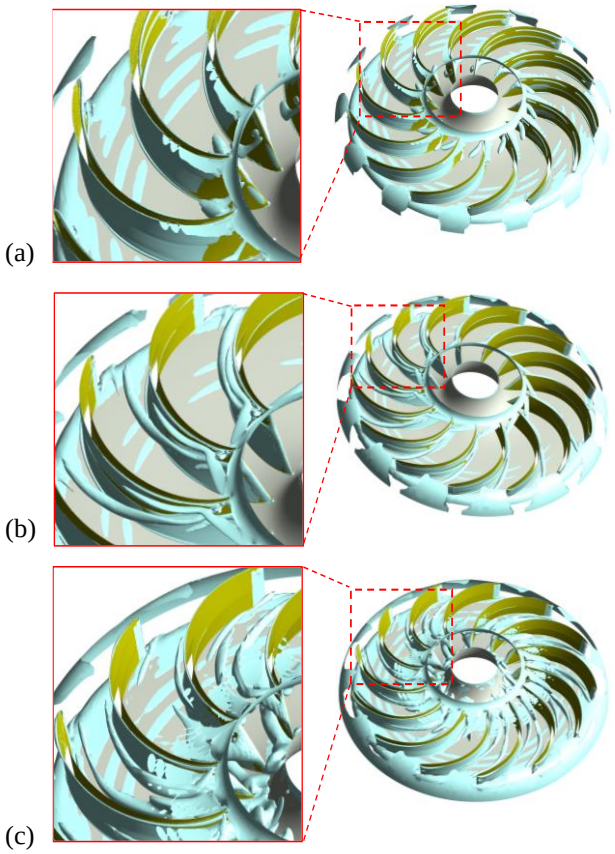

Fig. 19 Typical vortex structures occurring in the forward vane region at different flow conditions (iso-surface of the Q-criterion = 500,000 s^{-2}): (a) 0.5Q_{BEP}, (b) Q_{BEP} and (c) 1.3Q_{BEP}

structure is mainly distributed near the leading edge, extending from Span 0.5 to Span 0.1. At the best efficiency operation, the vortex structure extends the whole passage roughly with the forward vane curvature, mainly located near the Span 0.9 surface. Under overload conditions, the number of long vortex structures in the channel increases, and the deviation between the vortex tube extension path and vane curvature increases. Meanwhile, there are many broken vortices in the inlet region.

4.4.4. Second-Stage Runner

Figure 20 shows the contour of the $S_{D'}$ generation and velocity vector distribution on the meridian plane of the second-stage runner at different flow conditions. By comparing Fig. 20 and Fig. 14, it can be observed that the significant difference in the distribution of $S_{D'}$ entropy between the second-stage runner and the first-stage runner is that the entropy dissipation in the blade channel of the second-stage runner is smaller than that of the first-stage runner. Meanwhile, under partial load, the$S_{D'}$ generated by the vortex at the inlet of the second-stage runner is closer to the hub region. It is speculated that there are two possible factors that may cause the difference. First, the inlet flow conditions of the runner are different. Second, the outlet of the second-stage runner is connected to the draft tube with a long straight cone section, unlike the first-stage runner facing an axial to radial turn immediately at the outlet.

Figure 21 shows the contour of the $S_{D'}$ generation and streamline distribution on the spanwise plane of the second-stage runner under different flow conditions. Similar to the first-stage runner shown in Fig. 14, the $S_{D'}$ generation is mainly located in the striking flow region of the leading edge, the squeezing region in the blade channel, and the wake region of the tailing edge. Under partial load of 0.5Q_{BEP}, the second-stage runner has a large amount of $S_{D'}$ generation at the inlet of all spanwise planes due to the existence of reflux zone. At best efficiency operation, the $S_{D'}$ production near blade inlet is higher on Span 0.1 because the placement angle of the blades does not match the flow angle. At overload operation, the $S_{D'}$ generation in the blade channel of the second-stage runner is smaller than that of the first runner. The above details indicate that the second-stage runner is more adaptable to the flow angle under overload conditions; which also leads to its poor adaptability under partial load conditions. Therefore, it is observed in Fig. 9 that the $S_{D'}$ of the second-stage runner is much larger than that of the first-stage runner at partial load, while the reverse is true under overload conditions.

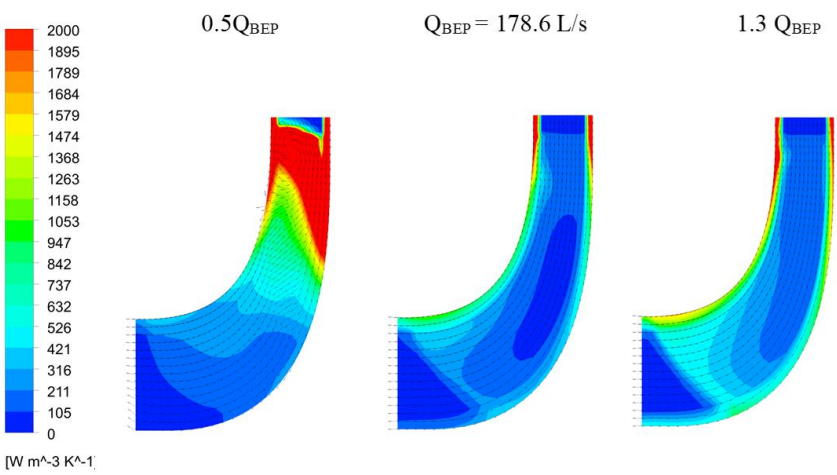

Fig. 20 Contours of $S_{D'}$ and the velocity vector distribution on the meridian plane of the second-stage runner under different flow conditions

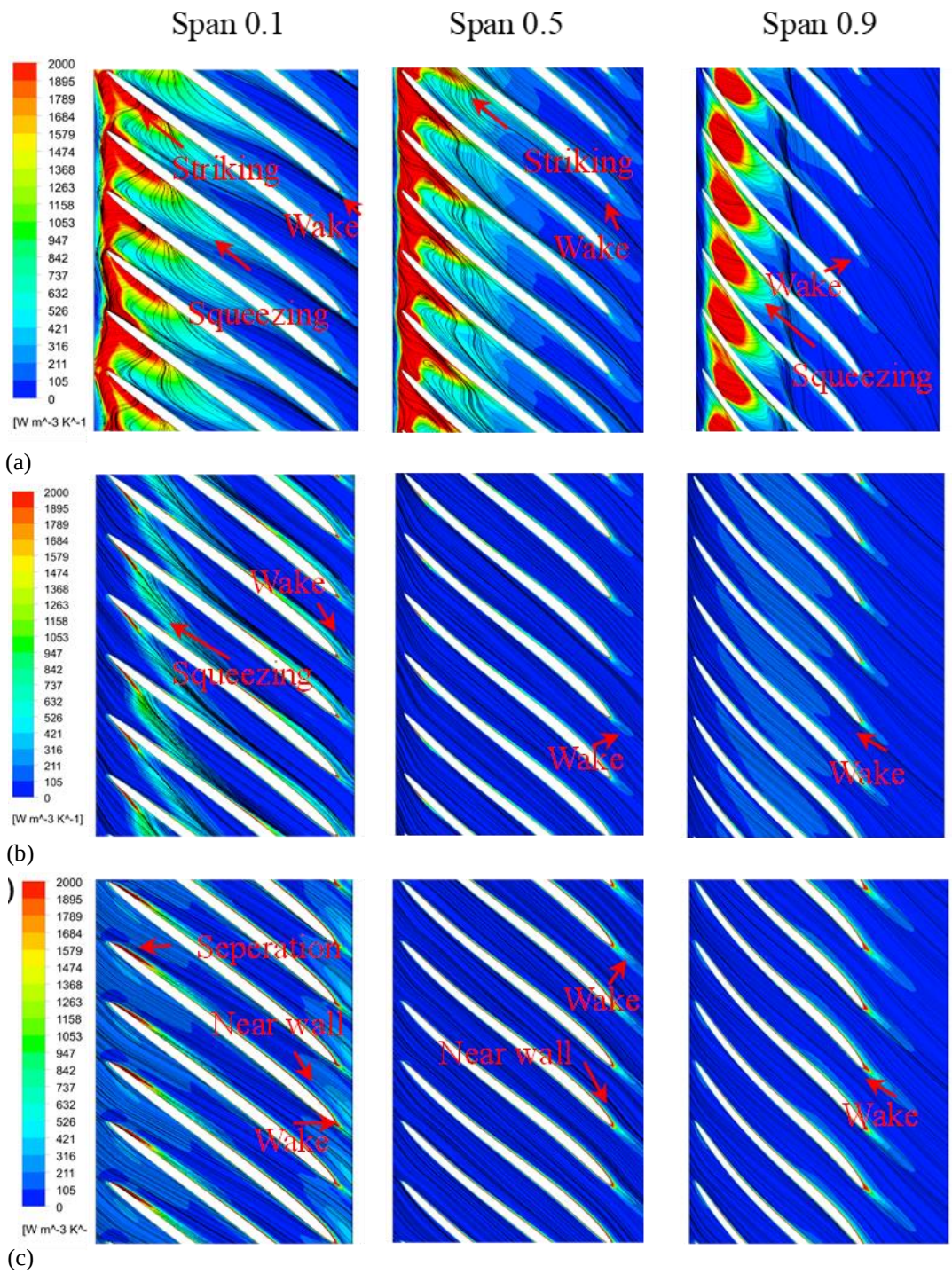

Fig. 21 Contour of the $S_{D'}$ generation and streamlines in Span 0.1, 0.5 and 0.9 of the second-stage runner at different flow conditions: (a) 0.5Q_{BEP}, (b) Q_{BEP}, (c) 1.3Q_{BEP}

Figure 22 shows the entropy production caused by the wall effect on the second-stage runner blade surface under different flow conditions. Comparing Fig. 22 and Fig. 16, the S_W production pattern of the runner blades remains basically consistent. It was found that local detachment near the runner blades will reduce the S_W production on the blade surface (corresponding to the dark blue area on the blade surface in Fig. 15 and Fig. 22). Therefore, in Fig. 11, it was observed that the S_W production under partial loads showed a trend of first increasing and then decreasing with a smaller change amplitude, because the evolution of the detachment structure with the flow velocity was not linearly changing. Further comparison between Fig. 14 and Fig. 20, as well as Fig. 15 and Fig. 21, shows that the $S_{D'}$ generation in the blade channel of the second-stage runner is smaller than that of the first-stage runner, and the degree of detachment near the second-stage runner blade surface is weaker than that of the first-stage runner. Therefore, the wall friction dissipation is greater for the second-stage runner than for the first-stage runner as shown in Fig. 11. Yu et al. (2022) also discovered similar phenomena in which a stable attached cavity can wrap the blade and reduce friction resistance, thereby reducing the wall entropy production value. Under overload conditions, due to the increase in the velocity of the mainstream fluid, the

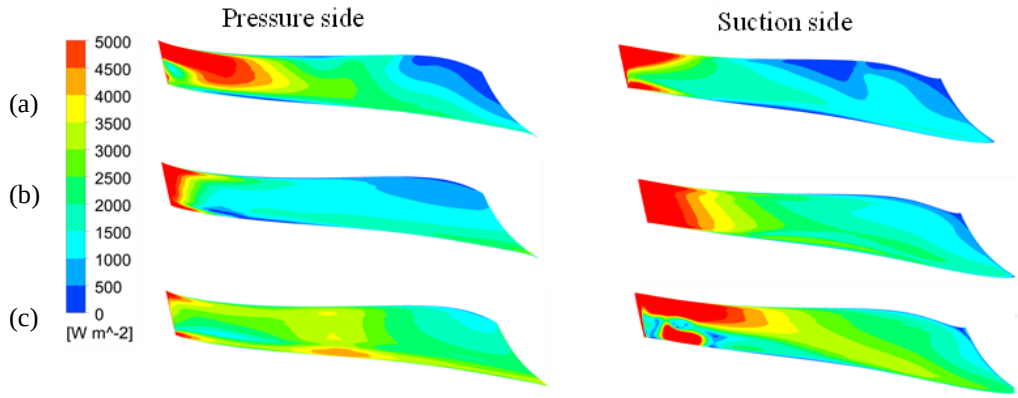

Fig. 22 Entropy production caused by the wall effect of the second-stage runner blades under different flow conditions: (a) 0.5Q$_{BEP}$, (b) Q$_{BEP}$, and (c) 1.3Q$_{BEP}$

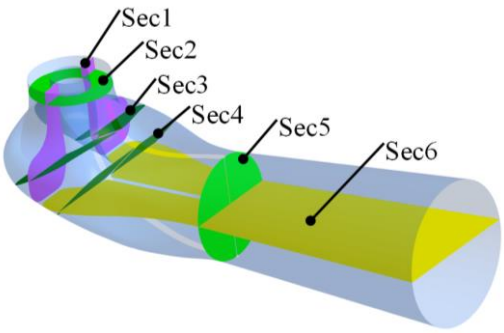

Fig. 23 Position of the sampling surfaces

detachment phenomenon in the channel weakens, and the contribution of the wake of the separation at the leading edge to the S_W generation increases. Consequently, the S_W generation shows a linear increasing trend with an increasing flow rate.

4.4.5. Draft Tube

To clearly observe the details of the $S_{D'}$ generation in the draft tube domain, six sampling surfaces are provided and depicted in Fig. 23. Figure 24 shows the contour of the $S_{D'}$ and streamlines on different sampling surfaces at different flow conditions. The larger $S_{D'}$ generation is distributed in the conical tube region behind the outlet of the second-stage runner and the region near the bottom partition. Because the main shaft is set in the center of the channel, no vortex rope forms in the conical tube region, such as the pump turbine running (Tao & Wang, 2021). Under a partial load of 0.5Q$_{BEP}$, there are two vortices at the bottom corner on the sampling surface of Sec1 as shown in Fig. 24(a); The blockage effect of vortices forces the fluid to flow downward along the walls on both sides, forming a large amount of $S_{D'}$ generation. Then, the fluid turns around the corner and flows forward in a swirling flow pattern. When it flows to the partition, it collides with the partition and interacts with adjacent vortices, resulting in a large amount of $S_{D'}$ generation. At the best efficiency operation, the volume of the vortices at the bottom corner on the sampling surface of Sec1 as shown in Fig. 24(b) shrinks, and the fluid in the conical tube

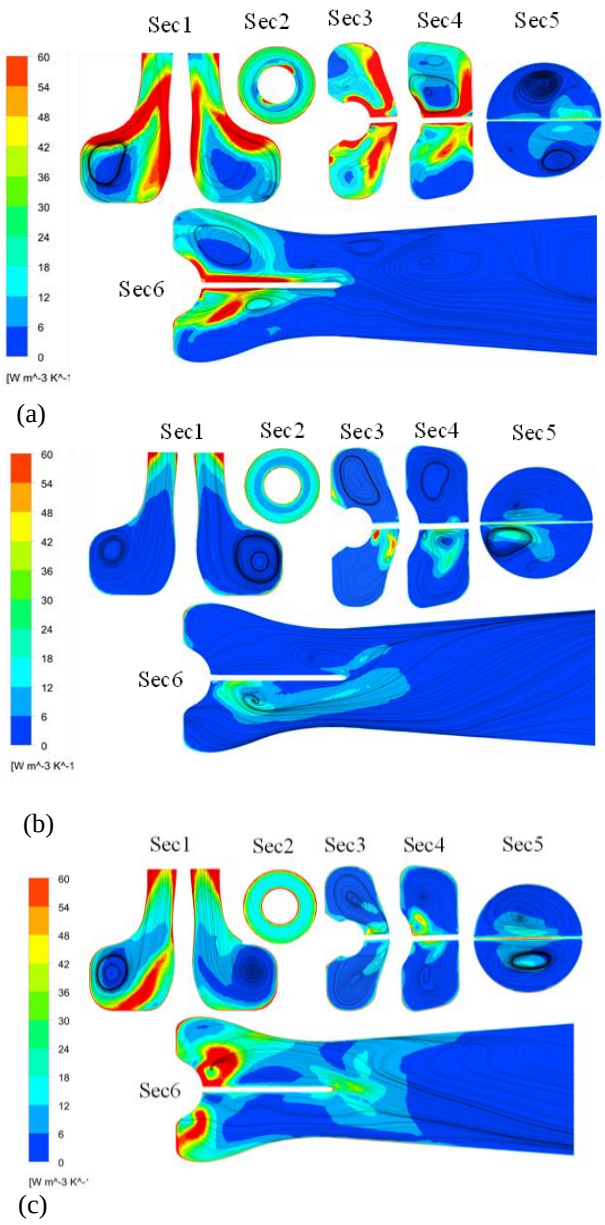

Fig. 24 Contours of the $S_{D'}$ generation and streamlines on different sampling surfaces of the draft tube under different flow conditions: (a) 0.5Q$_{BEP}$, (b) Q$_{BEP}$, and (c) 1.3Q$_{BEP}$

region can flow smoothly to the bottom, resulting in a decrease in the $S_{D'}$ generation. The streamlines on the sampling surface of Sec6 become orderly, and the $S_{D'}$ generation on both sides of the partition decreases. When the flow rate increases to the overload condition as shown in Fig. 24(c), the impact between the fluid and the bottom corner increases. Moreover, there is a large $S_{D'}$ generation at the corner. Meanwhile, the vortices were distributed symmetrically on both sides of the bottom partition. From Sec3 to Sec5, the distribution of entropy production on both sides of the partition gradually becomes symmetrical.

5. CONCLUSION

In this work, the energy dissipation within a vertical single suction two-stage centrifugal pump in a turbine model was calculated using entropy generation theory. The reasons for the energy dissipation of each component were explored by flow field analysis including streamlines, and entropy generation rate contours. In this study, the following conclusions can be obtained:

(1) The energy dissipation based on entropy generation theory in TVPAT mainly comes from turbulent fluctuation and wall friction, and the losses caused by viscous effects are relatively small and negligible. Due to the large number of blades in the PAT runner in this study, which is 18 blades, the energy loss caused by wall friction exceeds that caused by turbulent fluctuation at optimal operating conditions, with specific values of 58.18% and 43.63%, respectively.

(2) The turbulent entropy dissipation mainly comes from the runners; High turbulent entropy dissipations are mainly located in the striking flow region of the leading edge, the flow squeezing region in the blade channel, the wake region of the tailing edge and the near wall of the blades. The fundamental cause of turbulent entropy dissipation in the runner region is the mismatch between the placement angle of the blade and the liquid flow angle. The distribution area of wall friction on the pressure side of the blade leading edge decreases with an increasing flow rate, while the opposite pattern is observed on the suction side. The distribution of the wall friction production on the middle and rear wall surfaces of the blade is influenced by the local detachment in the channel.

(3) The return channel contributes significantly to turbulent energy dissipation under overload operations. In the forward vane region, the largest turbulent entropy generation is located in the inlet because the upstream flow direction is forced to change from axial to radial here; Especially under an overload operation of $1.3Q_{BEP}$, the flow pattern in the inlet region deteriorates further, forming a large number of broken vortices. In the backward vane region, turbulent entropy dissipation mainly occurs in the striking flow region of the leading edge and the wake region of the tailing edge.

(4) The turbulent entropy generation of the spiral case is positively correlated with the flow, and mainly comes from the fixed guide vane channel and near-wall region. The turbulent entropy generation from the daft tube has the least variation ranging from 5.92% to 10.57%. The larger $S_{D'}$ generation is distributed in the conical tube region behind the runner outlet and the region near the bottom partition.

ACKNOWLEDGEMENTS

This work was supported by the Natural Science Foundation Funded Projection of Heilongjiang Province (Grant No. ZD2020E002).

CONFLICT OF INTEREST

The authors declare that they have no conflict of interest. Informed consent was obtained from all individual participants included in the study.

AUTHORS CONTRIBUTION

T. P. Chen: Conceptualization, Methodology, Writing-original draft. **X. Z. Wei, R. S. Bie:** Conceptualization, Methodology, Supervision. **Y. Li, T. Zhang, Y. X. Liu:** Software, Validation, Writing - review & editing.

REFERENCES

Barbarelli, S., Amelio, M., Florio, G., & Scornaienchi, N. M. (2017). Procedure selecting pumps running as turbines in micro hydro plants. *Energy Procedia*, *126*, 549-556. https://doi.org/10.1016/j.egypro.2017.08.282

Binama, M., Su, W. T., Li, X. B., Li, F. C., Wei, X. Z., & An, S. (2017). Investigation on pump as turbine (PAT) technical aspects for micro hydropower schemes: A state-of-the-art review. *Renewable and Sustainable Energy Reviews*, *79*, 148-179. http://dx.doi.org/10.1016/j.rser.2013.11.030

Barrio, R., Fernández, J., Parrondo, J., & Blanco, E. (2010). *Performance prediction of a centrifugal pump working in direct and reverse mode using computational fluid dynamics.* International conference on renewable energies and power quality, Granada, Spain. https://doi.org/10.1016/j.renene.2017.02.045

Blomquist, C. A., Frigo, A. A., & Degnan, J. R. (1979). *Evaluation of advanced hydraulic turbomachinery for underground pumped hydroelectric storage. Part 2. Two-stage regulated pump/turbines for operating heads of 1000 to 1500 m.* Argonne National Lab., United States, USA. https://doi.org/10.2172/6716879

Duan. L., Wu. X., Ji. Z., & Fang. Q. (2015). Entropy generation analysis on cyclone separators with different exit pipe diameters and inlet dimensions. *Chemical Engineering Science*, *138*, 622-633. https://doi.org/10.1016/j.ces.2015.09.003

Derakhshan, S., & Nourbakhsh, A. (2008a). Experimental study of characteristic curves of centrifugal pumps

working as turbines in different specific speeds. *Experimental Thermal and Fluid Science*, *32*, 800-7. https://doi.org/10.1016/j.expthermflusci.2007.10.004

Derakhshan, S., & Nourbakhsh, A. (2008b). Theoretical, numerical and experimental investigation of centrifugal pumps in reverse operation. *Experimental Thermal and Fluid Science*, *32*, 1620-7. https://doi.org/10.1016/j.expthermflusci.2008.05.004

Fernandez, J., Blanco, E., Parrondo, J., Stickland, M. T., & Scanlon, T. J. (2004). Performance of a centrifugal pump running in inverse mode. *Proceedings of the Institution of Mechanical Engineers, Part A: Journal of Power and Energy*, *218*, 265-71. https://doi.org/10.1243/0957650041200632

Ghorani, M. M., Haghighi, M. H. S., Maleki, A., & Riasi, A. (2020). A numerical study on mechanisms of energy dissipation in a pump as turbine (PAT) using entropy generation theory. *Renewable Energy*, *162*, 1036-1053. https://doi.org/10.1016/j.renene.2020.08.102

Gong, R. Z., Qi, N. M., Wang, H. J., Chen, A. L., & Qin, D. Q. (2017). Entropy production analysis for S-characteristics of a pump turbine. *Journal of Applied Fluid Mechanics*, *10*, 1657-1668. https://doi.org/10.18869/acadpub.jafm.73.243.27675

Günther, T., Schulze, M., & Theisel, H. (2016). Rotation invariant vortices for flow visualization. *IEEE Transactions on Visualization and Computer Graphics*, *22*, 817-826. https://doi.org/10.1109/TVCG.2015.2467200

Gong, R., Wang, H., Chen, L., Li, D., Zhang, H., & Wei, X. (2013). Application of entropy production theory to hydro-turbine hydraulic analysis. *Science China Technological Sciences*, *56*, 1636-1643. https://doi.org/10.1007/s11431-013-5229-y

Huang, S., Qiu, G., Su, X., Chen, J., & Zou, W. (2017). Performance prediction of a centrifugal pump as turbine using rotor-volute matching principle. *Renewable Energy*, *108*, 64-71. https://doi.org/10.1016/j.renene.2017.02.045

Hou, H., Zhang, Y., Li, Z., Jiang, T., Zhang, J., & Xu, C. (2016). Numerical analysis of entropy production on a LNG cryogenic submerged pump. *Journal of Natural Gas Science and Engineering*, *36*, 87-96. https://doi.org/10.1016/j.jngse.2016.10.017

Herwig, H., & Kock, F. (2007). Direct and indirect methods of calculating entropy generation rates in turbulent convective heat transfer problems. *Heat and mass transfer*, *43*(3), 207-215. https://doi.org/10.1007/s00231-006-0086-x

International Electrotechnical Commission (1999). *IEC60193-1999, Hydraulic turbines, storage pumps and pump turbines-model acceptance tests*. Geneva, Switzerland.

Jain, S. V., & Patel, R. N. (2014). Investigations on pump running in turbine mode: A review of the state-of-the-art. *Renewable and Sustainable Energy Reviews*, *30*, 841-868. https://doi.org/10.1016/j.rser.2013.11.030

Kock, F., & Herwig, H. (2004). Local entropy production in turbulent shear flows: a high-Reynolds number model with wall functions. *International Journal of Heat and Mass Transfer*, *47*, 2205-2215. https://doi.org/10.1007/s11630-006-0159-7

Li, X. J., Ouyang, T., Lin, Y. P., & Zhu, Z. (2023). Interstage difference and deterministic decomposition of internal unsteady flow in a five-stage centrifugal pump as turbine. *Physics of Fluids, 35,* 045136. https://doi.org/10.1063/5.0150300

Li, X. J., Jiang, Z. W., Zhu, Z. C., Si, Q., & Li, Y. (2018). Entropy generation analysis for the cavitating head-drop characteristic of a centrifugal pump. *Journal of Mechanical Engineering Science*, *232*(24), 4637-4646. https://doi.org/10.1177/0954406217753458

Lin, T., Li, X., Zhu, Z., Xie, J., Li, Y., & Yang, H. (2021). Application of enstrophy dissipation to analyze energy loss in a centrifugal pump as turbine. *Renewable Energy*, *163*, 41-55. https://doi.org/10.1016/j.renene.2020.08.109

Lee, J., Moshfeghi, M., Hur, N., & Yoon, I. S. (2016). Flow analysis in a return channel of a multi-stage centrifugal pump. *Journal of Mechanical Science and Technology*, *30*(9), 3993-4000. https://doi.org/10.1007/s12206-016-0811-4

Li, D., Gong, R., Wang, H., Xiang, G., Wei, X., & Qin, D. (2016). Entropy production analysis for hump characteristics of a pump turbine model. *Chinese Journal of Mechanical Engineering*, *29*, 803-812. https://doi.org/10.3901/CJME.2016.0414.052

Maleki, A., Ghorani, M. M., Haghighi, M. H. S., & Riasi, A. (2020). Numerical study on the effect of viscosity on a multistage pump running in reverse mode. *Renewable Energy*, *150*, 234-254. https://doi.org/10.1016/j.renene.2019.12.113

Nautiyal, H., Varun, V., Kumar, A., Yadav, S. Y. S, (2011). Experimental investigation of centrifugal pump working as turbine for small hydropower systems. *Energy Science and Technology*, *1*, 79-86. https://doi.org/10.3968/j.est.1923847920110101.006

Nautiyal, H., & Kumar, V. A. (2010). Reverse running pumps analytical, experimental and computational study: a review. *Renewable and Sustainable Energy Reviews*, *14*, 2059-67. https://doi.org/10.1016/j.rser.2010.04.006

Menter, F. R. (1994). Two-equation eddy-viscosity turbulence models for engineering applications. *AIAA journal*, *32*(8), 1598-1605. https://doi.org/10.2514/3.12149

Pugliese, F., Fontana, N., Marini, G., & Giugni, M. (2021). Experimental assessment of the impact of number of

stages on vertical axis multi-stage centrifugal PATs. *Renewable Energy*, *178*, 891-903. https://doi.org/10.1016/j.renene.2021.06.132

Pei, J., Meng, F., Li, Y., Yuan, S., & Chen, J. (2016). Effects of distance between impeller and guide vane on losses in a low head pump by entropy production analysis. *Advances in Mechanical Engineering*, *8*, 1-11. https://doi.org/10.1177/1687814016679568

Qian, B., Chen, J. P., Wu, P., Wu, D. Z., Yan, P., & Li, S. Y. (2019). *Investigation on inner flow quality assessment of centrifugal pump based on Euler head and entropy production analysis.* IOP IOP Conference Series: Earth and Environmental Science, *240*, 92001. https://doi.org/10.1115/1.4047231

Sanghirun, W., & Asvapoositkul, W. (2023). Energy losses assessment of smallholder farmers' surface water irrigation pumps in south and southeast asia using entropy generation principle. *Journal of applied fluid mechanics*, *16*, 2023-2040. https://doi.org/10.47176/jafm.16.10.1851

Shehata, A. S., Saqr, K., Xiao, Q., Shehadeh, M. F., & Day, A. (2016). Performance analysis of wells turbine blades using the entropy generation minimization method. *Renewable Energy*, *86*, 1123-1133. https://doi.org/10.1016/j.renene.2015.09.045

Singh, P., & Nestmann, F. (2010). An optimization routine on a prediction and selection model for the turbine operation of centrifugal pumps. *Experimental Thermal and Fluid Science*, *34*, 152-64. https://doi.org/10.1016/j.expthermflusci.2009.10.004

Tao, R., & Wang, Z. (2021). Comparative numerical studies for the flow energy dissipation features in a pump-turbine in pump mode and turbine mode. *Journal of Energy Storage*, *41*, 102835. https://doi.org/10.1016/j.est.2021.102835

Wang, T., Wang, C., Kong, F., Gou, Q., & Yang, S. (2017). Theoretical, experimental, and numerical study of special impeller used in turbine mode of centrifugal pump as turbine. *Energy*, 130, 473-485. https://doi.org/10.1016/j.energy.2017.04.156

Williams, A. A. (1996). Pumps as turbines for low cost micro hydro power. *Renew Energy*, *9*, 1227-34. https://doi.org/10.1016/0960-1481(96)88498-9

Williams, A. (1994). The turbine performance of centrifugal pumps: a comparison of prediction methods. *Proceedings of the Institution of Mechanical Engineers, Part A: Journal of Power and Energy*, *208*, 59-66. https://doi.org/10.1243/PIME_PROC_1994_208_009_02

Xia, L., Cheng, Y., You, J., Zhang, X., Yang, J., & Qian, Z. (2017). Mechanism of the S-shaped characteristics and the runaway Instability of Pump-Turbines. *Journal of Fluids Engineering*, *139*(3), 031101. https://doi.org/10.1115/1.4035026

Yu, A., Li, L., Ji, J., & Tang, Q. (2022). Numerical study on the energy evaluation characteristics in a pump turbine based on the thermodynamic entropy theory. *Renewable Energy*, *195*, 766-779. https://doi.org/10.1016/j.renene.2022.06.077

Yang, Y., Zhou, L., Shi, W., He, Z., Han, Y., & Xiao, Y. (2021). Interstage difference of pressure pulsation in a three-stage electrical submersible pump. *Journal of Petroleum Science and Engineering*, *196*, 107653. https://doi.org/10.1016/j.petrol.2020.107653

Yang, S. S., Derakhshan, S., & Kong, F. Y. (2012). Theoretical, numerical and experimental prediction of pump as turbine performance. *Renewable Energy*, *48*, 507-513. https://doi.org/10.1016/j.renene.2012.06.002

Zhu, B., Han, W., Tai, Z., & Chen, Y. (2023). Flow evolution and energy loss mechanism in accidental shutdown process of a large submersible mixed-flow pump system. *Journal of Applied Fluid Mechanics*, *16*, 947-959. https://doi.org/10.47176/jafm.16.05.1550